Large and Tunable Photothermoelectric Effect in Single-Layer MoS$_2$

Michele Buscema,* Maria Barkelid, Val Zwiller, Herre S. J. van der Zant, Gary A. Steele,* and Andres Castellanos-Gomez*

Kavli Institute of Nanoscience, Delft University of Technology, Lorentzweg 1, 2628 CJ Delft, The Netherlands

S *Supporting Information*

ABSTRACT: We study the photoresponse of single-layer MoS$_2$ field-effect transistors by scanning photocurrent microscopy. We find that, unlike in many other semiconductors, the photocurrent generation in single-layer MoS$_2$ is dominated by the photothermoelectric effect and not by the separation of photoexcited electron−hole pairs across the Schottky barriers at the MoS$_2$/electrode interfaces. We observe a large value for the Seebeck coefficient for single-layer MoS$_2$ that by an external electric field can be tuned between -4×10^2 and -1×10^5 μV K^{-1}. This large and tunable Seebeck coefficient of the single-layer MoS$_2$ paves the way to new applications of this material such as on-chip thermopower generation and waste thermal energy harvesting.

KEYWORDS: *Molybdenum disulfide nanosheets, scanning photocurrent microscopy, photoresponse, photothermoelectric effect, Seebeck coefficient*
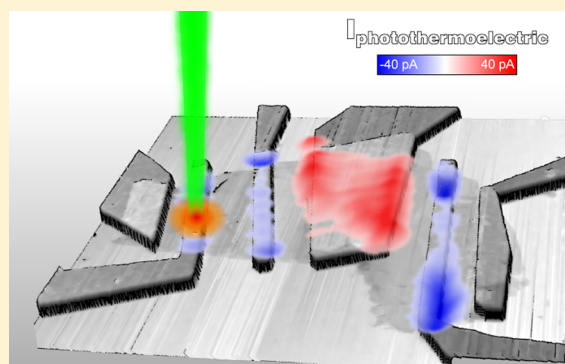
The experimental realization of graphene[1,2] has opened the door not only to study exciting new phenomena but also to explore a whole new family of two-dimensional materials with complementary properties.[3,4] For example, atomically thin semiconductor materials with a large bandgap are very interesting for electronic and optoelectronic applications where the lack of bandgap in graphene is hampering its applicability. Single-layer MoS$_2$ presents a large intrinsic bandgap (1.8 eV),[5−9] large in-plane mobility (200−500 cm^2 V^{-1} s^{-1})[6] and remarkable mechanical properties.[10,11] These properties are of great interest for sensors,[12] flexible circuits[13,14] and optoelectronic devices.[15−17]

Recent works studying the optoelectronic properties of MoS$_2$ have shown that the photoresponse of externally biased MoS$_2$-based phototransistors is driven by the change in conductivity upon illumination.[15−17] The photovoltaic effect in MoS$_2$ devices has also been reported with metallic electrodes that generate large Schottky barriers (SBs) and poor electrical contacts.[18,19] These previous works made use of either an externally applied or a built-in electric field to separate the photogenerated carriers.

Here, we employ scanning photocurrent microscopy to study the photocurrent generation mechanism in single-layer MoS$_2$ transistors with no Schottky barriers and no external bias. We demonstrate that in contrast to previous studies the photo-thermoelectric effect dominates the photoresponse in our devices. From our observations, we estimate the electric-field modulation of the Seebeck coefficient for single-layer MoS$_2$, finding a large value that can be tuned by more than 2 orders of magnitude.

The devices consist of a single-layer MoS$_2$ flake, deposited onto a Si/SiO$_2$ (285 nm) substrate by mechanical exfoliation.[3] Electrical contacts have been fabricated by standard electron-beam lithography and subsequent deposition of a Ti(5 nm)/Au(50 nm) layer. A combination of atomic force microscopy (AFM), Raman spectroscopy, and optical microscopy[20] (see Supporting Information) has been used to characterize the MoS$_2$ samples. Figure 1a shows an AFM image of a field effect transistor (FET) fabricated with a single-layer MoS$_2$ flake. The line trace in Figure 1b shows that the height of the flake is around 0.9 nm in agreement with values previously reported in the literature.[20] Raman spectroscopy was also employed to further characterize the deposited MoS$_2$ layers.[21−23] As reported by C. Lee et al.[21] the frequency difference between the two most prominent Raman peaks depends monotonically on the thickness and it can therefore be used to accurately determine the number of MoS$_2$ layers. The Raman spectroscopy measurements confirm that our devices are single-layer MoS$_2$ (see Supporting Information). In order to increase the quality of the electrical contacts, the samples were annealed at 300 °C for two hours in a Ar/H$_2$ flow (500 sccm/100 sccm).[6]

Figure 1c shows source−drain characteristics of the single-layer device at different gate voltages shown in Figure 1(a). The current versus voltage relationship remains almost linear for a broad bias range, indicating that the conduction through the device is not dominated by Schottky barriers (SBs), which is in agreement with previous results by Radisavljevic et al. using
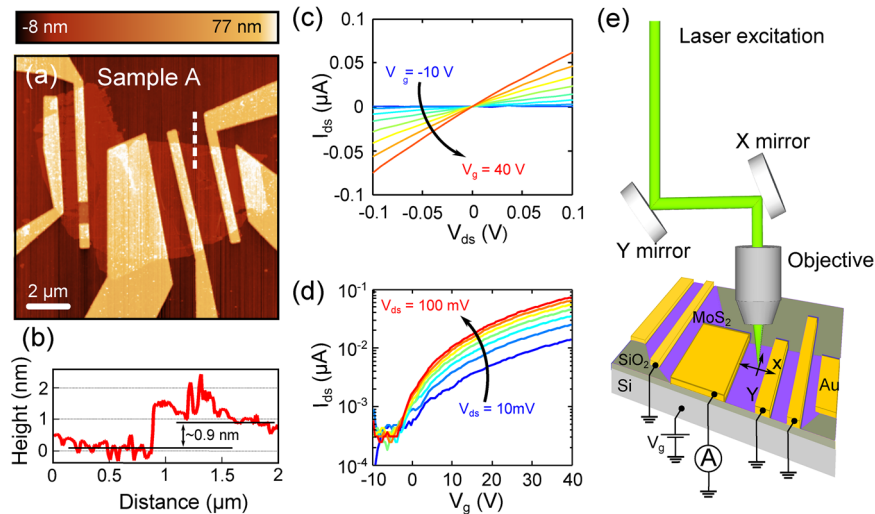
Figure 1. (a) Atomic force microscopy image of one of the studied devices, showing the MoS_2 flake and the electrodes used to make electrical contact. (b) Line profile over the dashed line in panel a showing the MoS_2 flake height. (c) Source−drain current versus source−drain bias characteristics measured at different gate voltages. (d) Electrical transport characteristic of a MoS_2-based FET device (source−drain current versus gate voltage) measured at different source−drain bias. For both panels c and d, the channel length is 1.6 μm and width is 4.5 μm. (e) Schematic of the SPCM setup showing the excitation path and electric circuit used to perform SPCM measurements.
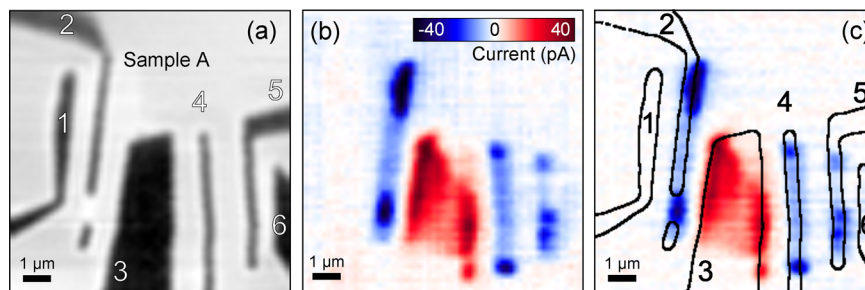
Figure 2. (a) Spatial map of the intensity of the reflected light from the device (white corresponds to low reflection). Electrodes have been numbered for clarity. (b) Photocurrent image of the MoS_2 FET. The colorscale in the inset gives the photocurrent value. (c) Superposition of the photocurrent map (from (b), same colorscale) and contours of the electrodes as obtained from the light reflection map. The scale bars are always 1 μm. Reflection and photocurrent measurements are performed simultaneously with electrode number 3 connected to a current to voltage amplifier while the other electrodes are connected to ground. Excitation is given by a CW laser, λ = 532 nm, P = 1 μW, spot waist radius ∼400 nm. The region of the flake from the right edge of electrode 2 to the right edge of electrode 3 is composed by multiple layers of MoS_2 (see Figure S3 in the Supporting Information for a more detailed description). No current is seen flowing from electrode 1 or 6 because of poor contact between those with the underlying MoS_2 flake.

similar electrode materials and annealing conditions.[6] Moreover, variable temperature transport experiments on MoS_2 using low work function electrodes (Ti and Sc) demonstrated a Schottky barrier height slightly larger than k_BT at room temperature.[24]

This is also consistent with recent density functional theory simulations and experimental work that demonstrate that Ti/MoS_2 interfaces provide ohmic contacts.[25,26] Figure 1d shows various gate traces measured at different source−drain voltages. The device shows a pronounced n-type behavior with a current on/off ratio exceeding 10^3 and a mobility of ∼0.85 cm^2 V^{-1} s^{-1}, that is characteristic of single-layer MoS_2 FETs fabricated on SiO_2 surfaces.[6,12,15,26−28]

To spatially resolve the local photoresponse of the MoS_2−FET device, we performed scanning photocurrent microscopy (SPCM) in a home-built scanning confocal microscope (see Figure 1e) with excitation provided by a continuous wave green laser (λ = 532 nm) and a supercontinuum tunable source (at λ = 750 nm see Supporting Information for details).[29] In our experimental setup, the intensity of the reflected laser light

(Figure 2a) and the photocurrent (Figure 2b) generated in the device are simultaneously recorded at every position during the scanning of the laser spot. It is thus possible to superimpose the two images to accurately determine where the photocurrent is generated (Figure 2c).

The gray scale image in Figure 2c shows the reflection image and the color-scale shows the simultaneously measured current flowing through the device at zero bias (electrode 3 is connected to a current-to-voltage amplifier while all other electrodes are connected to ground). As it can be seen (e.g., by looking at electrode 3), there is photogenerated current at zero bias even when the laser spot is placed inside the area of the electrodes, micrometers away from the electrode edges, corresponding to distances up to 10 times larger than the full-width at half-maximum of the laser spot intensity profile. This is in striking contrast with several earlier findings on photocurrent on graphene,[30,31] which is localized at the interface between the graphene flake and the metal electrodes. In these previous works, the zero-bias photocurrent generation mechanism was attributed to the electron−hole separation at
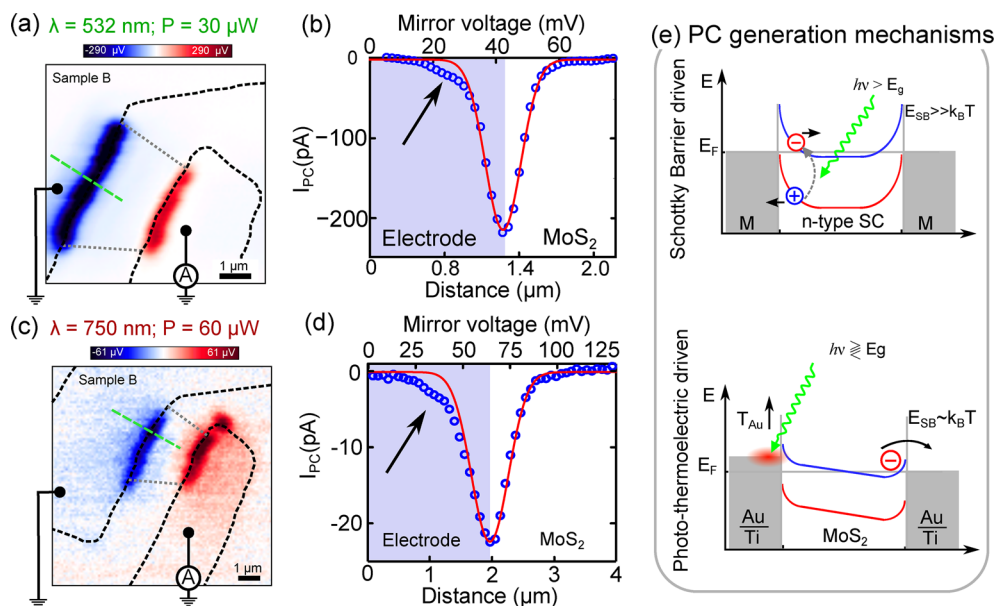
Figure 3. Photovoltage map of a single layer MoS$_2$ FET using an excitation wavelength of 532 nm (a) and 750 nm (c). (b,d) Photocurrent profile across the linecut in panels a,b (open blue circles). The solid red line is a Gaussian fit of the data and the arrow points at the photocurrent tail generated when the laser spot is scanned over the electrode. The shaded blue area represents the electrode area as determined by the reflection signal. (d) Schematic of photoresponse mechanism in a typical metal−semiconductor−metal device. (e) Schematic of the photoresponse mechanism in a device dominated by photothermoelectric effect. The conduction band is drawn in blue while the valence band is drawn in red.

the SBs. This mechanism, however, cannot explain the presence of a photogenerated current when the laser is illuminating the metal electrodes, far from the electrode edges where SBs would be located.

The observation of photocurrent with the laser positioned deep inside the metal electrode suggests that the principal photocurrent generation mechanism in our device is different from photocurrent generation by the separation of photo-excited electron−hole pairs due to the localized electric field at the metal/semiconductor interface. This observation is also consistent with our conclusions from the data in Figure 1b that the SBs are not relevant for the transport characteristics of the device.

In order to gain a deeper insight into the photoresponse mechanism of single-layer MoS$_2$ FETs, we have performed scanning photocurrent measurements using different illumination wavelengths. Figure 3a shows a photoresponse map acquired with green (λ = 532 nm, $h\nu$ = 2.33 eV) illumination. The photovoltage is obtained by dividing the measured photocurrent by the device resistance, measured under the same illumination conditions. A line profile of the photocurrent measured along the dashed green line in Figure 3a is presented in Figure 3b as open blue circles. The solid red line is a Gaussian fit to the data corresponding to a diffraction limited laser spot. Notice that there is a significant photocurrent tail generated when the laser is scanned over the electrode (arrow in Figure 3b). This is again inconsistent with a response shifted into the MoS$_2$ region, as would be expected for a photovoltaic response from Schottky barriers.

Figure 3c shows a photoresponse map acquired with red (λ = 750 nm, $h\nu$ = 1.65 eV) illumination. The photovoltage is calculated as in Figure 3a. Note that the photovoltage under green illumination is larger because of the lower reflectance (and thus higher absorption) of the gold electrodes for this wavelength. The observation of photoresponse even for photon energies lower than the bandgap (Figure 3c) cannot be

explained by separation of photoexcited electron−hole pairs (see Figure 3e, top panel). Moreover, previous photo-conductivity measurements in MoS$_2$ transistors under large source−drain bias have not shown any significant photo-response for excitation wavelength above 700 nm (or below 1.77 eV).[15,32] This indicates that sub-bandgap impurity states are either not present or do not contribute to photocurrents, even in the presence of a large extraction bias, precluding sub-bandgap states as a possible source of photocurrent in Figure 3c. From these considerations, we conclude that the generation of photocurrent with excitation energies below the bandgap cannot be ascribed to a photovoltaic effect.

Interestingly, for above-bandgap illumination, where photo-voltaic effects could play a role, the photocurrent images show characteristics that are qualitatively very similar to those for below bandgap illumination. A line profile of the photocurrent measured along the dashed green line in Figure 3c is presented in Figure 3d in the same fashion as in Figure 3b to facilitate the comparison. The qualitative agreement, and in particular the tail of photocurrent when the laser is focused over the metal, suggests that the photogeneration mechanism is not dominated by photovoltaic effects even for above-bandgap excitation. This hypothesis is also consistent with a lack of the gate dependence of the SPCM images at above bandgap excitation energies (λ = 532 nm). In particular, the position of the maximum photocurrent in the photovoltaic effect would be expected to shift with the gate voltage, an effect also not observed in our devices (see Supporting Information Figure S5c). This also suggests that the main mechanism for photocurrent generation, even with above-bandgap illumination, is not the photovoltaic effect.

The negligible role of the SBs in the conductance of the devices, the strong measured photocurrent inside the area of the electrodes whose position is gate-independent and the observation of qualitatively identical photoresponse between sub and above-bandgap illumination all suggest that photo-

voltaic effects cannot be responsible for the photoresponse observed here. Instead, we propose that the photoresponse in our device arises from a strong photothermoelectric effect.[33−37] In the photothermoelectric effect (Figure 3e, bottom panel), a temperature gradient arising from light absorption generates a photothermal voltage across a junction between two materials with different Seebeck coefficient. This photothermovoltage can drive current through the device. This mechanism is consistent with our observation of strong photocurrents when the laser is focused on the metallic electrodes and also explains the presence of localized and intense photocurrent spots at the edges of the electrodes where the laser absorption is increased and the heat dissipation is reduced. Moreover, it would also explain the stronger photocurrent in the electrode area in Figure 2 where the MoS_2 underneath the electrode is more than one layer thick which reduces the thermal coupling with the substrate and thus increases the local temperature of the electrode (see Figures S3 and S8 in the Supporting Information).

The photothermoelectric generation of current can be understood as follows: the local absorption of the laser creates a local heating of the junction between the gold and the MoS_2 layer. This local heating of the junction is translated into a voltage difference (ΔV_{PTE}), which will drive current through the device, by the difference between the Seebeck coefficients of the MoS_2 flake (S_{MoS_2}) and the electrodes (S_{TiAu}) and the local increase of the junction temperature (ΔT) (see Supporting Information). This ΔT can be modeled as the temperature difference of the locally heated gold electrode (T_{Au}) and a part of the MoS_2 flake which is distant from the junction (T_{MoS_2}).

$$\Delta V_{PTE} = (S_{MoS_2} - S_{TiAu})\Delta T$$
$$= (S_{MoS_2} - S_{TiAu})(T_{MoS_2} - T_{TiAu}) \quad (1)$$

We have further studied the gate dependence of the photothermoelectric effect in single layer MoS_2 by measuring the electrical transport characteristics of single MoS_2 devices while the laser spot is placed at a location with high photoresponse. For illumination wavelengths with a photon energy higher than the bandgap, the threshold voltage is shifted toward very negative values (see Figure 4a) not reachable without leading to gate leakage. It is therefore preferable to use illumination wavelengths with photon energy below the bandgap to minimize this photoconductivity effect.

Figure 4b shows the photothermoelectric voltage (ΔV_{PTE}) measured for a single-layer MoS_2 device at different gate voltages. The photothermoelectic voltage is the intercept with the voltage bias (V_{ds}) axis of the IV characteristic of the devices measured under sub-bandgap illumination. By decreasing the gate voltage below the threshold voltage, the photothermo-electric voltage shows a substantial increase. As the ΔV_{PTE} is proportional to the difference in the Seebeck coefficients and the temperatures of the AuTi electrodes and MoS_2 flake (expression 1), the observed behavior can be attributed to the expected gate dependence of the Seebeck coefficient of MoS_2.

At a microscopic level, the Seebeck effect is due to three microscopic processes that are in dynamic equilibrium with each other.[38,39] The first process is the diffusion of electrons due to a steady state temperature gradient along a conductor; this process is proportional to the specific heat capacity of the electrons in the conductor. The second process is the variation
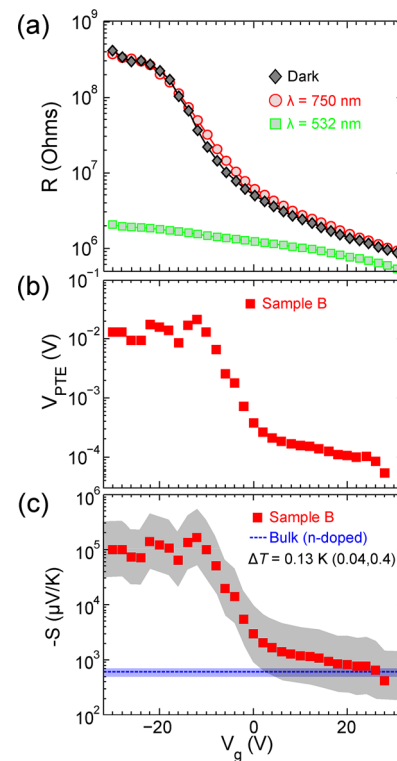
Figure 4. (a) Resistance of a single-layer MoS_2 device as a function of gate voltage in dark state and with the laser spot placed on the MoS_2/electrode interface. Two different illumination wavelengths have been used (532 and 750 nm). (b) Photothermoelectric voltage for a single-layer MoS_2 device measured with the laser spot (λ = 750 nm) placed on the MoS_2/electrode interface. (c) Estimated Seebeck coefficient versus gate voltage. The values are calculated from eq 1 using the measured photovoltage (symbols). The gray shaded area is the uncertainty due to the uncertainty in the estimation of the temperature gradient. The dashed light blue line corresponds to the Seebeck coefficient value of bulk MoS_2 with experimental uncertainty (shaded light blue area). The saturation effect at negative gate values is due to the high resistance of the device, leading to a current value below the noise floor of the current-to-voltage amplifier.

of the chemical potential with temperature; this will modify the concentration of electrons along the temperature gradient and, therefore, induce a diffusive flux of electrons. The third process is the phonon-drag; as phonons diffuse from the warm side of the conductor to the cold side, they can scatter and drag along electrons. This process is proportional to the electron−phonon coupling and the specific heat of phonons. All these processes depend on or influence the density of states in the conductor. Therefore, they are bound to show a behavior which is dependent on an external gate electric field (see Supporting Information for more details).

As it is difficult to experimentally determine microscopic properties such as the energy dependent density of states in a given sample, the Seebeck coefficient is often parametrized in terms of the conductivity of the sample using the Mott relation[40−43]

$$S = \frac{\pi^2 k_B^2 T}{3e} \frac{d\ln(\sigma(E))}{dE}\bigg|_{E=E_F} \quad (2)$$

where k_B is the Boltzmann constant, T is the temperature, e is the electron charge, $\sigma(E)$ is the conductivity as a function of energy, and the derivative is evaluated at the Fermi energy E_F.

Using expression 2 we estimate the maximum Seebeck coefficient in our device (see Supporting Information) to be on the order of $-0.2 \times 10^5 \, \mu V \, K^{-1}$, roughly an order of magnitude lower than the value we estimate from our measurements (see below). This discrepancy could arise from the fact that expression 2 is based on the assumption that the conductor is a metal or a degenerate semiconductor, which is not the case for a single flake of MoS_2 near depletion.

According to expression 1 the Seebeck coefficient of MoS_2 can be determined from ΔV_{PTE} and the estimate of the temperature gradient across the $AuTi/MoS_2$ junction. Notice that the Seebeck coefficient of AuTi is negligible with respect to that of MoS_2 and no gate dependence is expected. To estimate the increase of temperature induced by the laser illumination, we have performed a finite elements analysis calculation, taking into account the reflections losses in the objective and at the surface of the sample and the absorbed intensity through the material according to $(I = I_0[1 - \exp(-\alpha d)])$ where α is the absorption coefficient of the material and d is its thickness. With the employed laser excitation ($\lambda = 750$ nm, $I_0 = 60 \, \mu W$, and $R_{spot} \approx 500$ nm), if we assume that all the energy delivered by the laser is converted into heat we obtain $\Delta T_{AuTi/MoS2} \approx 0.13$ K (see Supporting Information). Figure 4c shows the estimated values; the experimental data are represented by squares while the shaded area represents the uncertainty in the estimation of the Seebeck coefficient deriving from an assumed uncertainty of a factor of 3 in the calculation of the temperature gradient (that is $\Delta T_{AuTi/MoS2}$ in between 0.04 and 0.4 K). The Seebeck coefficient value for bulk MoS_2 (between -500 and $-700 \, \mu V$ K^{-1}) is also plotted to facilitate the comparison.[44] A negative value of the Seebeck coefficient is expected for n-type semiconductors.

The obtained value for the Seebeck coefficient is remarkably large and varies strongly with the gate voltage from $-2 \times 10^2 \sim -1.5 \times 10^3 \, \mu V/K$ at high doping levels (high positive gate) to $-3 \times 10^4 \sim -3 \times 10^5 \, \mu V/K$ at low doping levels (high negative gate). Notice that at negative gate voltages, the Seebeck coefficient value saturates. This is due to the large resistance of the device at negative gate voltages that yields to a measured photocurrent that can be below the noise floor of the current amplifier (leading to the observed saturation in the estimated Seebeck coefficient).

The Seebeck coefficient that we observe for single-layer MoS_2 is orders-of-magnitude larger than that of graphene (± 4 to $100 \, \mu V \, K^{-1}$),[33,34,45−47] semiconducting carbon nanotubes ($\sim -300 \, \mu V \, K^{-1}$),[48] organic semiconductors ($\sim 1 \times 10^3 \, \mu V$ K^{-1})[49] and even than materials regularly employed for thermopower generation such as Bi_2Te_3 ($\pm 150 \, \mu V \, K^{-1}$).[50,51] On the other hand, the presented Seebeck coefficient is comparable with other materials such as MnO_2 powder ($20 \times 10^3 \sim 40 \times 10^3 \, \mu V \, K^{-1}$)[52] and Fe_2O_3 ($\pm 10 \times 10^3 \, \mu V \, K^{-1}$).[53] In addition, the wide gate tunability of the Seebeck coefficient can be useful for applications such as on-chip power generation and thermoelectric nanodevices. These applications include, but are not limited to, energy harvesting of waste thermal energy of other processes[54,55] and to the possibility of developing autonomously powered devices.[56,57] In all these applications, the tunability of the Seebeck coefficient represents an efficient way of optimizing device performances.[56,57]

In summary, using sub-bandap illumination, we have demonstrated a clear and strong photothermoelectric effect arising from the large mismatch between the Seebeck coefficients of the MoS_2 and of the electrodes. Furthermore, the identical qualitative characteristics of the photocurrent images for above bandgap illumination suggests that the photothermal effect is also the dominant mechanism for photocurrent generation here as well, and that photovoltaic effects seem not to play a significant role. We estimated the Seebeck coefficient for single-layer MoS_2, finding a large value which can be tuned by an external electric field between $\sim -4 \times 10^2$ and $\sim -1 \times 10^5 \, \mu V \, K^{-1}$. This value is 70−25000 times larger than the values reported for graphene. From these results, we expect that single-layer MoS_2 could be an interesting complement to graphene in applications requiring a material with a large and tunable Seebeck coefficient, such as thermoelectric nanodevices or energy harvesting.

■ ASSOCIATED CONTENT

⑤ Supporting Information

Supporting Information includes detailed explanation of the materials and methods employed, optical images of the studied devices, relationship between morphology and photocurrent data, photocurrent line profiles acquired at different gate voltages, photocurrent maps at different excitation wavelengths, the finite element analysis carried out to estimate the laser induced increase of temperature in the devices, power dependence of the photoresponse, estimation of the laser beam spot size and theoretical background of the Seebeck coefficient gate dependence. This material is available free of charge via the Internet at http://pubs.acs.org.

■ AUTHOR INFORMATION

Corresponding Author

*E-mail: (M.B.) M.Buscema@tudelft.nl; (G.A.S.) G.A.Steele@ tudelft.nl; (A.C.-G.) a.castellanosgomez@tudelft.nl.

Notes

The authors declare no competing financial interest.

■ ACKNOWLEDGMENTS

■ REFERENCES

(1) Novoselov, K.; Geim, A.; Morozov, S.; Jiang, D.; Zhang, Y.; Dubonos, S.; Grigorieva, I.; Firsov, A. *Science* **2004**, *306* (5696), 666−669.

(2) Novoselov, K.; Geim, A.; Morozov, S.; Jiang, D.; Grigorieva, M. I. K. I. V.; Dubonos, S.; Firsov, A. *Nature* **2005**, *438* (7065), 197−200.

(3) Novoselov, K.; Jiang, D.; Schedin, F.; Booth, T.; Khotkevich, V.; Morozov, S.; Geim, A. *Proc. Natl. Acad. Sci. U.S.A.* **2005**, *102* (30), 10451.

(4) Coleman, J. N.; Lotya, M.; O'Neill, A.; Bergin, S. D.; King, P. J.; Khan, U.; Young, K.; Gaucher, A.; De, S.; Smith, R. J. *Science* **2011**, *331* (6017), 568−571.

(5) Ayari, A.; Cobas, E.; Ogundadegbe, O.; Fuhrer, M. S. *J. Appl. Phys.* **2007**, *101* (1), 014507.

(6) Radisavljevic, B.; Radenovic, A.; Brivio, J.; Giacometti, V.; Kis, A. *Nat. Nanotechnol.* **2011**, *6* (3), 147−150.

(7) Mak, K. F.; Lee, C.; Hone, J.; Shan, J.; Heinz, T. F. *Phys. Rev. Lett.* **2010**, *105* (13), 136805.

(8) Splendiani, A.; Sun, L.; Zhang, Y.; Li, T.; Kim, J.; Chim, C. Y.; Galli, G.; Wang, F. *Nano Lett.* **2010**, *10* (4), 1271−1275.

(9) Eda, G.; Yamaguchi, H.; Voiry, D.; Fujita, T.; Chen, M.; Chhowalla, M. *Nano Lett.* **2011**, *11* (12), 5111−5116.

(10) Bertolazzi, S.; Brivio, J.; Kis, A. *ACS Nano* **2011**, *5* (12), 9703−9709.

(11) Castellanos-Gomez, A.; Poot, M.; Steele, G. A.; van der Zant, H. S. J.; Agraït, N.; Rubio-Bollinger, G. *Adv. Mater.* **2012**, *24* (6), 772−775.

(12) Li, H.; Yin, Z.; He, Q.; Li, H.; Huang, X.; Lu, G.; Fam, D. W. H.; Tok, A. I. Y.; Zhang, Q.; Zhang, H. *Small* **2012**, *8* (1), 63−67.

(13) Pu, J.; Yomogida, Y.; Liu, K.-K.; Li, L.-J.; Iwasa, Y.; Takenobu, T. *Nano Lett.* **2012**, *12* (8), 4013−4017.

(14) He, Q.; Zeng, Z.; Yin, Z.; Li, H.; Wu, S.; Huang, X.; Zhang, H. *Small* **2012**, *8* (19), 2994−2999.

(15) Yin, Z.; Li, H.; Jiang, L.; Shi, Y.; Sun, Y.; Lu, G.; Zhang, Q.; Chen, X.; Zhang, H. *ACS Nano* **2012**, *6* (1), 74−80.

(16) Lee, H. S.; Min, S.-W.; Chang, Y.-G.; Park, M. K.; Nam, T.; Kim, H.; Kim, J. H.; Ryu, S.; Im, S. *Nano Lett.* **2012**, *12* (7), 3695−3700.

(17) Choi, W.; Cho, M. Y.; Konar, A.; Lee, J. H.; Cha, G.-B.; Hong, S. C.; Kim, S.; Kim, J.; Jena, D.; Joo, J.; Kim, S. *Adv. Mater.* **2012**, *24* (43), 5832−5836.

(18) Marcio Fontana, T. D.; Boyd, A. K.; Rinzan, M.; Liu, A. Y.; Paranjape, M.; Barbara, P. 2012, arXiv:1206.6125 [cond-mat.mtrl-sci].

(19) Shanmugam, M.; Durcan, C. A.; Yu, B. *Nanoscale* **2012**, DOI: 10.1039/c2nr32394j.

(20) Castellanos-Gomez, A.; Agrait, N.; Rubio-Bollinger, G. *Appl. Phys. Lett.* **2010**, *96* (21), 213116−3.

(21) Lee, C.; Yan, H.; Brus, L. E.; Heinz, T. F.; Hone, J.; Ryu, S. *ACS Nano* **2010**, *4* (5), 2695−2700.

(22) Korn, T.; Heydrich, S.; Hirmer, M.; Schmutzler, J.; Schüller, C. *App. Phys. Lett.* **2011**, *99*, 102109.

(23) Late, D. J.; Liu, B.; Matte, H. S. S. R.; Rao, C. N. R.; Dravid, V. P. *Adv. Funct. Mater.* **2012**, *22* (9), 1894−1905.

(24) Das, S.; Chen, H.-Y.; Penumatcha, A. V.; Appenzeller, J. *Nano Lett.* **2013**, *13* (1), 100−105.

(25) Popov, I.; Seifert, G.; Tománek, D. *Phys. Rev. Lett.* **2012**, *108* (15), 156802.

(26) Ghatak, S.; Pal, A. N.; Ghosh, A. *ACS Nano* **2011**, *5* (10), 7707−7712.

(27) Castellanos-Gomez, A.; Barkelid, M.; Goossens, A. M.; Calado, V. E.; van der Zant, H. S. J.; Steele, G. A. *Nano Lett.* **2012**, *12* (6), 3187−3192.

(28) Liu, H.; Ye, P. D. *IEEE Electron Device Lett.* **2012**, *33* (4), 546−548.

(29) Buchs, G.; Barkelid, M.; Bagiante, S.; Steele, G. A.; Zwiller, V. *J. Appl. Phys.* **2011**, *110*, 074308.

(30) Xia, F.; Mueller, T.; Golizadeh-Mojarad, R.; Freitag, M.; Lin, Y.-m.; Tsang, J.; Perebeinos, V.; Avouris, P. *Nano Lett.* **2009**, *9* (3), 1039−1044.

(31) Park, J.; Ahn, Y. H.; Ruiz-Vargas, C. *Nano Lett.* **2009**, *9* (5), 1742−1746.

(32) Mak, K. F.; Lee, C.; Hone, J.; Shan, J.; Heinz, T. F. *Phys. Rev. Lett.* **2010**, *105* (13), 136805.

(33) Xu, X.; Gabor, N. M.; Alden, J. S.; van der Zande, A. M.; McEuen, P. L. *Nano Lett.* **2009**, *10* (2), 562−566.

(34) Gabor, N. M.; Song, J. C. W.; Ma, Q.; Nair, N. L.; Taychatanapat, T.; Watanabe, K.; Taniguchi, T.; Levitov, L. S.; Jarillo-Herrero, P. *Science* **2011**, *334* (6056), 648−652.

(35) Song, J. C. W.; Rudner, M. S.; Marcus, C. M.; Levitov, L. S. *Nano Lett.* **2011**, *11* (11), 4688−4692.

(36) St-Antoine, B.; Ménard, D.; Martel, R. *Nano Res.* **2012**, *5* (2), 73−81.

(37) Sun, D.; Aivazian, G.; Jones, A. M.; Ross, J. S.; Yao, W.; Cobden, D.; Xu, X. *Nat. Nanotechnol.* **2012**, *7* (2), 114−118.

(38) MacDonald, D. K. C. *Thermoelectricity: an introduction to the principles*; Wiley: New York, 1962.

(39) Ashcroft, N. W.; Mermin, N. D. *Solid state physics*; Saunders College: Philadelphia, 1976.

(40) Mott, N. F.; Jones, H. *The theory of the properties of metals and alloys*; The Clarendon Press: Oxford, 1936.

(41) Bhushan, B. *Springer Handbook of Nanotechnology*; Springer: New York, 2007; Chapter 12.

(42) Heremans, J. P.; Jovovic, V.; Toberer, E. S.; Saramat, A.; Kurosaki, K.; Charoenphakdee, A.; Yamanaka, S.; Snyder, G. J. *Science* **2008**, *321* (5888), 554−557.

(43) Nolas, G. S.; Sharp, J.; Goldsmid, J. *Thermoelectrics: Basic Principles and New Materials Developments* Springer: New York, 2001.

(44) Mansfield, R.; Salam, S. A. *Proc. Phys. Soc. B* **1953**, *66* (5), 377−385.

(45) Seol, J. H.; Jo, I.; Moore, A. L.; Lindsay, L.; Aitken, Z. H.; Pettes, M. T.; Li, X.; Yao, Z.; Huang, R.; Broido, D.; Mingo, N.; Ruoff, R. S.; Shi, L. *Science* **2010**, *328* (5975), 213−216.

(46) Grosse, K. L.; Bae, M.-H.; Lian, F.; Pop, E.; King, W. P. *Nat. Nanotechnol.* **2011**, *6* (5), 287−290.

(47) Wang, Z.; Xie, R.; Bui, C. T.; Liu, D.; Ni, X.; Li, B.; Thong, J. T. L. *Nano Lett.* **2011**, *11* (1), 113−118.

(48) Small, J. P.; Perez, K. M.; Kim, P. *Phys. Rev. Lett.* **2003**, *91* (25), 256801.

(49) Pernstich, K. P.; Rossner, B.; Batlogg, B. *Nat. Mater.* **2008**, *7* (4), 321−325.

(50) Fleurial, J. P.; Gailliard, L.; Triboulet, R.; Scherrer, H.; Scherrer, S. *J. Phys. Chem. Solids* **1988**, *49* (10), 1237−1247.

(51) Bassi, A. L.; Bailini, A.; Casari, C. S.; Donati, F.; Mantegazza, A.; Passoni, M.; Russo, V.; Bottani, C. E. *J. App. Phys.* **2009**, *105* (12), 124307−9.

(52) FangFang, S.; Liming, W.; Liang, S. *Nanotechnology* **2012**, *23* (8), 085401.

(53) Gardner, R. F. G.; Sweett, F.; Tanner, D. W. *J. Phys. Chem. Solids* **1963**, *24* (10), 1183−1196.

(54) Bell, L. E. *Science* **2008**, *321* (5895), 1457−1461.

(55) Chowdhury, I.; Prasher, R.; Lofgreen, K.; Chrysler, G.; Narasimhan, S.; Mahajan, R.; Koester, D.; Alley, R.; Venkatasubramanian, R. *Nat. Nanotechnol.* **2009**, *4* (4), 235−238.

(56) Liang, W.; Hochbaum, A. I.; Fardy, M.; Rabin, O.; Zhang, M.; Yang, P. *Nano Lett.* **2009**, *9* (4), 1689−1693.

(57) Ohta, H.; Masuoka, Y.; Asahi, R.; Kato, T.; Ikuhara, Y.; Nomura, K.; Hosono, H. *Appl. Phys. Lett.* **2009**, *95* (11), 113505−3.